

See discussions, stats, and author profiles for this publication at: <https://www.researchgate.net/publication/272387718>

Solvothermal Synthesis of $\text{LiMn}_{1-x}\text{Fe}_x\text{PO}_4$ Cathode Materials: A Study of Reaction Mechanisms by Time-Resolved in Situ Synchrotron X-ray Diffraction

ARTICLE in THE JOURNAL OF PHYSICAL CHEMISTRY C · JANUARY 2015

Impact Factor: 4.77 · DOI: 10.1021/jp508600u

CITATIONS

3

READS

39

5 AUTHORS, INCLUDING:



Jianming Bai

Brookhaven National Laboratory

139 PUBLICATIONS 2,234 CITATIONS

SEE PROFILE



Jian Hong

Binghamton University

19 PUBLICATIONS 618 CITATIONS

SEE PROFILE



Jason Graetz

HRL Laboratories, LLC

109 PUBLICATIONS 2,875 CITATIONS

SEE PROFILE



Feng Wang

Brookhaven National Laboratory

46 PUBLICATIONS 967 CITATIONS

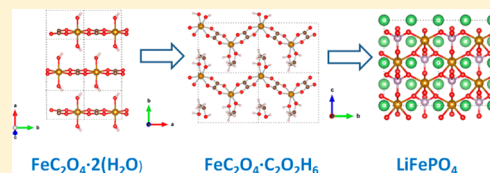
SEE PROFILE

Solvothermal Synthesis of $\text{LiMn}_{1-x}\text{Fe}_x\text{PO}_4$ Cathode Materials: A Study of Reaction Mechanisms by Time-Resolved in Situ Synchrotron X-ray Diffraction

Jianming Bai,^{*,†} Jian Hong,[‡] Haiyan Chen,[§] Jason Graetz,^{||,‡} and Feng Wang[‡][†]Photon Science Directorate and [‡]Sustainable Energy Technologies Department, Brookhaven National Laboratory, Upton, New York 11973, United States[§]Mineral Physics Institute, Stony Brook University, Stony Brook, New York 11794, United States

S Supporting Information

ABSTRACT: We applied time-resolved in situ synchrotron X-ray diffraction (XRD) to study the reaction processes and pathways during the solvothermal synthesis of the olivine-structured LiFePO_4 , LiMnPO_4 , and $\text{LiFe}_{0.4}\text{Mn}_{0.6}\text{PO}_4$ with ethylene glycol $\text{C}_2\text{H}_6\text{O}_2$ (EG) as the solvent by following the evolution of the crystal structures of the Fe/Mn-containing phases. We identified a stable intermediate phase in the synthetic reaction process of LiFePO_4 , viz., a ferrous oxalate EG complex ($\text{FeC}_2\text{O}_4 \cdot \text{C}_2\text{H}_6\text{O}_2$), and resolved its structure; thus, we established a two-step reaction mechanism involving dissolution–precipitation followed by interface-coupled dissolution–reprecipitation for the synthesis of LiFePO_4 . The synthetic reactions in an $\text{LiFe}_{0.4}\text{Mn}_{0.6}\text{PO}_4$ solid solution also followed a two-step process via the formation of a metastable intermediate phase bearing a structural similarity to $\text{FeC}_2\text{O}_4 \cdot \text{C}_2\text{H}_6\text{O}_2$ that, however, has a slightly larger unit-cell, indicating that the substitution of Fe by Mn occurred at the intermediate stage. In contrast, the reaction in the synthesis of LiMnPO_4 proceeds through a simple process of precipitation. Our findings provide important information for optimizing the synthesis of olivine cathode materials. The in situ XRD method we developed in this work offers a new way of exploring a wide range of solvothermal synthesis reactions, which is valuable for the rational design of new batteries.



INTRODUCTION

Lithium-ion batteries are the preferred energy-storage devices for portable electronics, and have become leading candidates of power sources for electric vehicles and grid-scale storage. For large-scale commercial usages, it is critical to develop cost-effective methods for synthesizing high-energy electrodes.

Olivine-type cathodes, LiMPO_4 ($\text{M} = \text{Fe}, \text{Mn}$), and their solid solutions are the most promising materials to replace traditional LiCoO_2 electrodes.^{1,2} LiFePO_4 (LFP) is known for its low cost, high thermal stability, and environmental benignity. Recent demonstrations of its high-power capability make it a preferred cathode for the new generation of lithium-ion batteries.^{3–7} However, the low working voltage of LFP, only 3.4 V versus Li^+/Li , deters its widespread application as the cathode in high-energy batteries.⁸ LiMnPO_4 is a promising candidate to replace LFP as the high-energy cathode; it has a specific capacity (171 mAh/g) equivalent to that of LFP, but a 0.7 V higher redox potential.^{9,10} However, its theoretical capacity rarely has been achieved, even in mild operating conditions, and slow progress has been made so far on improving its performance. This poor electrochemical performance primarily was attributed to poor electronic conductivity and to Jahn–Teller effects. Also, Mn^{2+} has radii much larger than that of Mn^{3+} , so causing a large change in volume during charge and discharge. Partial substitution of Mn by Fe in the olivine structure effectively improved the specific- and rate-

capabilities of LiMnPO_4 .^{11–13} With the introduction of Fe into LiMnPO_4 , the inactive $\text{Mn}^{3+}/\text{Mn}^{2+}$ redox pairs start to show electrochemical activity. Even though the Fe-substituted system has a theoretical energy density lower than that of pure LiMnPO_4 , it demonstrated improved reversible capacity, excellent rate performance, and also good cycle stability.¹¹

Traditionally, olivine-type cathode materials are prepared by solid-state synthesis at high temperatures. Recently, low-temperature hydrothermal synthesis has been used for preparing single-metal phosphates, LiFePO_4 or LiMnPO_4 , but rarely is it applied for synthesizing high-quality $\text{LiFe}_x\text{Mn}_{1-x}\text{PO}_4$ solid solutions.¹⁴ Solvothermal synthesis using ethylene glycol (EG) as the solvent turned out to be successful in producing an $\text{LiFe}_x\text{Mn}_{1-x}\text{PO}_4$ (LFMP) solid solution, which exhibited a reversible capacity as high as 153 mAh/g.¹⁵ Furthermore, the solvothermal method was used for tuning the LFP crystal to the desired orientation and morphology, thus achieving high-rate capability.¹⁶ For further improving the solvothermal method and extending its application to the synthesis of a higher-energy $\text{LiFe}_x\text{Mn}_{1-x}\text{PO}_4$ solid solution with an optimized Fe/Mn ratio and performance, it is critical to have a better understanding, at atomic levels, of the reaction mechanisms by monitoring the

Received: August 25, 2014

Revised: January 5, 2015

Published: January 9, 2015



structural evolution and the phase transitions occurring during the reaction process.

There are a few reports on studies of the reaction mechanism on the solvothermal synthesis of LFP.^{15,17} However, almost all measurements have been *ex situ*, *viz.*, recording the XRD patterns or acquiring the SEM and TEM images from products recovered from a solution that was heated to a targeted temperature and then cooled to room temperature. Because the real-time reaction processes during a solvothermal synthesis cannot be characterized from *ex situ* measurements, applying *in situ* techniques is deemed indispensable. Recently, we successfully developed *in situ* reactors and special techniques for studying the reaction mechanisms during the hydrothermal synthesis of LFP using *in situ* synchrotron X-ray powder diffraction (XRD). We were able to track the structural changes in the crystalline phases as a function of the reaction temperature and time, using high-quality *in situ* powder diffraction data.¹⁸ With further development, this technique can be applied to studies of solvothermal synthesis of various high-energy cathode materials.

In this work, we probed the reaction mechanisms of solvothermal synthesis of the single-metal phosphates, LFP, and LMP and of their solid solution, $\text{LiFe}_x\text{Mn}_{1-x}\text{PO}_4$, in EG solvent using time-resolved *in situ* X-ray powder diffraction. We followed a rigorous Rietveld refinement procedure for our quantitative structure analysis of time-resolved powder diffraction patterns. We extracted structural parameters, such as lattice parameters, bond lengths, and the effective coordination numbers of the metal-containing crystalline phases, along with their evolution as a function of reaction time and temperature, from XRD patterns and used them to expound a reaction pathway. During the synthesis of LFP, we identified an intermediate phase and solved its crystal structure. We established a two-step reaction mechanism involving a dissolution–precipitation from precursor to the intermediate phase, followed by an interface-coupled dissolution–reprecipitation from the intermediate to the final product. We subsequently employed this two-step reaction mechanism to explain the incorporation of Fe and Mn into the same lattice to form the LFMP solid solution. The experimental and analytical methods we developed probe the synthetic reactions in real time and thus provide valuable information to aid in optimizing reaction conditions to increase the yield of the desired phase, decrease the waste, lower costs, and ultimately tailor the material's properties.

■ EXPERIMENTAL SECTION

Synthesis. $\text{LiFe}_x\text{Mn}_{1-x}\text{PO}_4$ ($x = 0, 0.2, 0.4, 0.6, 0.8, 1$) powders were prepared by the solvothermal method with ferrous oxalate dihydrate ($\text{FeC}_2\text{O}_4 \cdot 2\text{H}_2\text{O}$), manganese acetate tetrahydrate ($\text{Mn}(\text{CH}_3\text{COO})_2 \cdot 4\text{H}_2\text{O}$), and lithium dihydrogen phosphate (LiH_2PO_4) (all from Sigma-Aldrich) in an ethylglycol solvent. This *ex situ* synthesis was carried out in a stainless steel reactor under autogenous pressure, filled to approximately 75% volume capacity. The starting materials were suspended in 40 mL of ethylene glycol and then were stirred vigorously for 12 h at room temperature. The solvothermal process was undertaken at 240 °C for 12 h in an oven, after which we slowly cooled the mixture to room temperature. After filtration, the prepared samples were washed with deionized water and ethyl alcohol, dried under vacuum at 100 °C for 1 h, and finally collected for *ex situ* characterization.

In Situ Solvothermal Synthesis. The configuration of the solvothermal reactor for the *in situ* XRD measurements was similar to that detailed in ref 18. Well-mixed slurry was injected into a one-end sealed quartz tube (0.7 mm interior diameter) and filled to 2–3 mm. A small heat-resistant plastic cylinder was inserted into the quartz tube as a plug to keep the precursor slurry in place. The quartz tube then was filled with ethyl glycol and connected to one end of a 1/16 in. Swagelok elbow. Enough ethyl glycol was added to the elbow assembly via its open end to minimize the amount of air trapped within it. The open end of the elbow then was sealed with a Swagelok cap and mounted to the goniometer of an X-ray diffractometer.

In situ XRD measurements were conducted at beamline X14A at the NSLS. The X-ray beam, about 0.5 mm (vertically) \times 1.0 mm (horizontally), was focused by a sagittal focusing monochromator. The wavelength of X-ray was tuned to 0.7744 Å. A silicon strip detector was mounted on the 2θ arm of a 6-circle Huber diffractometer, about 1400 mm from the sample. The detector has 640 channels, each of which covers 0.005° in 2θ . The XRD patterns were taken by scanning the 2θ arm at 2°/step. Each scan took about 5 min with a 2θ angular range from 5° to 45°.

We used an Omega air-process heater to heat the reactor. The heater's temperature was monitored by a k-type thermocouple mounted near the hot-air nozzle and controlled by a Yokogawa UP550 temperature-controller. We obtained a calibration curve by using a k-type thermocouple inside a quartz tube that was placed at the reactor's position to record the actual temperatures. In the *in situ* XRD measurements, the sample area in the reactor was uniformly heated. The sample's temperature was derived from the calibration curve and the recorded control temperature. To homogenize the reacting mixture, and reduce the effect of preferred orientation, the reactor was rotated continuously during the XRD measurement, thereby providing an averaged powder XRD pattern, suitable for structural refinement.

For the *in situ* synthesis of LiFePO_4 (LFP), we mixed iron oxalate dihydrate, ethyl glycol, and lithium dihydrate phosphate to form an orange slurry and injected it into the quartz tube. For $\text{Li}(\text{Fe},\text{Mn})\text{PO}_4$ (LFMP) and LiMnPO_4 (LMP), iron oxalate dihydrate and magnesium acetate tetrahydrate were used as the source for transition metals. Time-lapse XRD patterns then were acquired while the calibrated temperature was ramped up linearly from 30 to 240 °C in about 2 h, again controlled by software specially tailored for the experiment.

Morphology and Structural and Chemical Analysis.

We used an Hitachi S-4800 scanning electron microscope (SEM), equipped with a cold-field emission gun, for morphological and structural characterization. Transmission electron microscopy (TEM) and energy-dispersive X-ray spectroscopy measurements were taken on the intermediate phase identified in the synthetic process of LFP at 200 kV using a JEOL2100F microscope that is equipped with a Schottky field-emitter and an energy-dispersive X-ray spectrometer (Oxford Energy TEM 250).

■ RESULTS AND DISCUSSION

XRD and Electrochemical Characterization of $\text{LiFe}_x\text{Mn}_{1-x}\text{PO}_4$. Figure 1a,c shows the high-resolution synchrotron XRD patterns of the synthesized $\text{LiFe}_x\text{Mn}_{1-x}\text{PO}_4$ powders, with x values of 0.0, 0.2, 0.4, 0.6, 0.8, and 1.0. These patterns can be well indexed by an olivine structure without impurity phases. The lattice parameters extracted from the

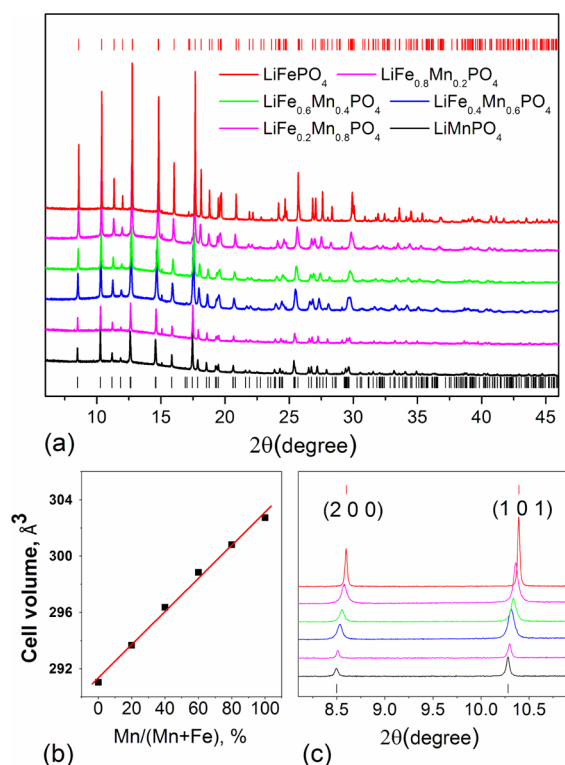


Figure 1. (a) X-ray diffraction patterns of the synthesized $\text{LiFe}_x\text{Mn}_{1-x}\text{PO}_4$ with $x = 0, 0.2, 0.4, 0.6, 0.8$, and 1 . The black and red bars show the refined peak positions of LMP and LFP, respectively. The X-ray wavelength was $\lambda = 0.77442 \text{ \AA}$. (b) The linear variation of the refined unit cell volume varies with the content of Mn and Fe ($R = 0.995$). (c) Enlarged local detail shows the linear shift of the first two Bragg peaks in the $\text{LiFe}_x\text{Mn}_{1-x}\text{PO}_4$ XRD patterns.

XRD patterns using the Rietveld refinement method revealed a linear relationship between the volume of the unit cell and the quantity of substituted Fe, as shown in Figure 1b, thus closely following Vegard's law. This provides evidence that Mn and Fe form a solid solution in the olivine structure. Based on SEM morphologic examination, the olivine crystallites are micron-sized in length, with aspect ratios ranging from ~ 1 to 7 , depending on the $\text{Fe}/(\text{Mn} + \text{Fe})$ ratio, indicating the promotion of anisotropic growth by the substitution of Mn with Fe (Figure S1 in Supporting Information).

To demonstrate the electrochemical activity of the solvothermally synthesized LFMP solid solutions, we tested the cycling performance of the as-synthesized materials. Figure S2 in Supporting Information shows the first two charge and discharge profiles of the $\text{LiFe}_x\text{Mn}_{1-x}\text{PO}_4$ ($x = 0, 0.8$, and 1) samples at a $C/10$ rate. LiFePO_4 exhibits one single redox plateau potential of $\sim 3.5 \text{ V}$, which is typical of LiFePO_4 , and the capacities reach 135 mAh/g at the $C/10$ rate. This capacity is comparable to those reported in the literature, while LiMnPO_4 and $\text{LiMn}_{0.8}\text{Fe}_{0.2}\text{PO}_4$ exhibit low capacities of <20 and $<40 \text{ mAh/g}$ at a voltage of about 4.3 V , respectively; this value is higher than the expected redox potential of $\text{Mn}^{2+/3+}$ (4.1 V) largely because of the polarization. The cycling profiles of the $\text{LiFe}_{0.4}\text{Mn}_{0.6}\text{PO}_4$, $\text{LiFe}_{0.6}\text{Mn}_{0.4}\text{PO}_4$, and $\text{LiFe}_{0.8}\text{Mn}_{0.2}\text{PO}_4$ exhibit voltage plateaus corresponding to both the $\text{Fe}^{2+/3+}$ (3.45 V) and $\text{Mn}^{2+/3+}$ (4.1 V) redox reactions. The $\text{LiFe}_{0.6}\text{Mn}_{0.4}\text{PO}_4$ sample has the highest capacity among these three samples at the first cycle. The first flat plateau at 3.48 V occurs after a sharp increase in voltage from the OCV 3.2 V , corresponding

to the oxidation of iron, Fe^{2+} to Fe^{3+} . The steep change of voltage (0.53 V) occurs before the second plateau (manganese oxidation from Mn^{2+} to Mn^{3+}) at 4.09 V , and then gradually increases to the cutoff voltage, resulting in a storage capacity of 100 mAh/g (Figure S3 in Supporting Information). The consequent discharge shows a similar two-plateau region for the M^{3+} to M^{2+} reduction ($\text{M} = \text{Mn}$ and Fe), resulting in a storage capacity of 80 mAh/g . This irreversible loss in capacity between the first charge and discharge reactions is about 20 mAh/g . In the subsequent cycles, the capacity of discharge and charge is similar and has a Coulombic efficiency of $>99\%$. For $\text{LiFe}_{0.8}\text{Mn}_{0.2}\text{PO}_4$ sample, the plateau from $\text{Mn}^{2+/3+}$ (4.1 V) redox reaction is very short and contributes less than 20 mAh/g to the total capacity.

The electrochemical tests confirm that both the $\text{Fe}^{2+/3+}$ (3.45 V) and $\text{Mn}^{2+/3+}$ (4.1 V) redox couples have electrochemical activity in the solvothermally synthesized solid solution samples.

Reaction Mechanisms by in Situ XRD. To understand the general reaction mechanisms involved in the ethylene glycol-mediated synthesis of olivine-type cathode materials, especially the formation of the bimetal phosphate solid solutions, we employed the in situ XRD technique to obtain the real-time structural evolution of materials involved in the entire reaction processes. In situ XRD studies first were undertaken on synthesizing two representative materials, LiFePO_4 and LiMnPO_4 , with only Fe or Mn cations participating in each reaction. Then, the same technique and procedures were applied to a model material, $\text{LiFe}_{0.4}\text{Mn}_{0.6}\text{PO}_4$, to reveal how a solid solution is formed in the presence of both Fe and Mn cations in the starting reactants. During an in situ XRD solvothermal synthesis, we followed the evolutions of the crystalline phases that contain Fe^{2+} , Mn^{2+} , or both from the starting materials to the final products so that the most relevant phase transformations were recorded and analyzed.

LiFePO_4 Synthesis. Structural Evolution. Figure 2 shows the XRD patterns collected in real time during the solvothermal

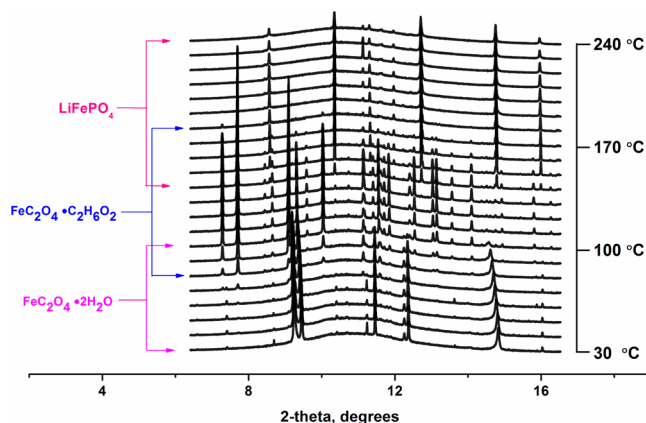


Figure 2. Time-resolved XRD patterns of the solvothermal synthesis of LiFePO_4 in an ethylene glycol solvent, from room temperature to $240 \text{ }^\circ\text{C}$. The X-ray wavelength is $\lambda = 0.77442 \text{ \AA}$. The presence of Fe-containing phase is indicated.

synthesis of LiFePO_4 in the temperature range from 30 to $240 \text{ }^\circ\text{C}$. According to the diffraction patterns recorded at room temperature, the primary crystalline phase in the mixed slurry is $\text{FeC}_2\text{O}_4 \cdot 2\text{H}_2\text{O}$, with LiH_2PO_4 as a minor one. Upon heating, the intensity of the diffraction peak associated with the main

phase ($\text{FeC}_2\text{O}_4 \cdot 2\text{H}_2\text{O}$) dropped gradually; new peaks emerged at about 60 °C, and their intensities grew with further heating. The new XRD pattern does not match any known phase in the newest ICDD-PDF database, indicating the presence of an unknown structure with lower symmetry. This intermediate phase was transformed quickly into the final product, LFP, at ~140 °C and was consumed completely at ~170 °C. The concentration of LFP grew with the rise in temperature until it leveled off up to 240 °C.

All the Fe-containing phases, including the intermediate phase, were identified, and their phase evolutions were obtained by quantitatively analyzing the diffraction patterns. As shown in Figure 3, the reaction process involves multiple phase

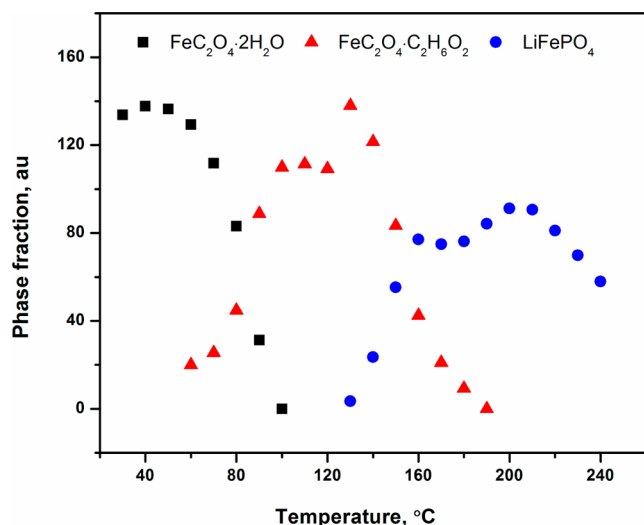


Figure 3. Normalized molar ratio of detectable crystalline phases during the solvothermal synthesis of LiFePO_4 from room temperature to 240 °C in ethylene glycol. Shown herein are the precursor phase, $\text{FeC}_2\text{O}_4 \cdot 2\text{H}_2\text{O}$ (black squares); the intermediate phase, $\text{FeC}_2\text{O}_4 \cdot \text{C}_2\text{H}_2\text{O}_6$ (red diamonds); and the product, LiFePO_4 (blue circles). Not shown are the small amounts of Li_3PO_4 and H_2LiPO_4 .

transitions during heating. At room temperature, the quantity of $\text{FeC}_2\text{O}_4 \cdot 2\text{H}_2\text{O}$ phase is high and drops gradually with heating, possibly as a result of its increased solubility at higher temperatures. A new phase starts to form at about 60 °C, entailing the rapid decomposition of $\text{FeC}_2\text{O}_4 \cdot 2\text{H}_2\text{O}$. The new intermediate phase, later identified as $\text{FeC}_2\text{O}_4 \cdot \text{C}_2\text{H}_2\text{O}_6$, is converted to the final product, LiFePO_4 , at 140 °C. The

conversion is completed at around 190 °C; there is significant decrease of the product during the further ramp-up of temperature to 240 °C. This is very likely related to the partial dissolution of the LFP particles after their first aggregation in the solvothermal synthesis, a feature previously observed by Lim et al. using laser diffraction.¹⁹ The LFP crystals, upon conversion from the intermediate phase, inherit the size and shape of their parent particles. The anisotropic surface energy with respect to different crystalline planes of LFP at the reaction temperature causes their partial dissolution, along with further morphology changes, thereby decreasing the sizes of the crystals of LFP, starting at 160 °C (Figure 13a); this in turn reduces the amount of the product. The total amount of the product phase starts to decline after the $\text{FeC}_2\text{O}_4 \cdot \text{C}_2\text{H}_2\text{O}_6$ phase is fully consumed at 190 °C. Li_3PO_4 also presents as a minor phase in the later stage of solvothermal synthesis and can be washed out of the final product because of its solubility in water.

Structure of the Intermediate Phase. The unknown intermediate phase observed in LiFePO_4 synthesis plays an important role, so we devoted some effort to solving its structure. Using a Parr reactor, we synthesized the intermediate phase from the same precursors under conditions identical to those determined from in situ reaction studies. Powder samples of intermediate phase were obtained by solvothermal synthesis at 130 °C for 3 h, followed by filtration and air drying. EDX characterization suggested that this intermediate phase consists of Fe and O, but not P. Subsequent examination of the powder by high-resolution XRD yielded structural information via XRD pattern indexing, LeBail fitting, and charge-flipping structure solution using TOPAS software.

The intermediate phase was indexed to a single orthorhombic phase with a space group $Pcab$, and lattice parameters of $a = 9.4687(1)$ Å, $b = 7.7711(1)$ Å, and $c = 19.53839(2)$ Å. The charge-flipping structural solution and subsequent Rietveld refinement provided atomic positions for Fe, C, and O, from which the bonding between atoms were revealed (Table 1). We then added the hydrogen atoms to the structure based on considering the refined C–C bond lengths and valence. The chemical formula of intermediate phase then was determined to be $\text{FeC}_2\text{O}_4 \cdot \text{C}_2\text{H}_2\text{O}_6$ from its atomic structure. Figure 4a displays the Rietveld refinement of the XRD pattern of $\text{FeC}_2\text{O}_4 \cdot \text{C}_2\text{H}_2\text{O}_6$, and Figure 4b is a ball-and-stick model of its unit cell. The XRD pattern of this intermediate phase is similar to a compound synthesized by Krasil'nikov et al. by mixing iron oxalate dihydrate in ethylene glycol and heating it

Table 1. Non-Hydrogen Atomic Positions of the $\text{FeC}_2\text{O}_4 \cdot \text{C}_2\text{H}_2\text{O}_6$ ^a

site	m	atom	Occ	x	y	z	Uiso (Å ²)
Fe1	8	Fe+2	1.00	0.54516(11)	0.56631(13)	0.86760(5)	0.010
O2	8	O-2	1.00	0.15730(31)	0.74040(39)	0.92692(18)	0.026
O3	8	O-2	1.00	0.22100(32)	0.88602(37)	0.80927(16)	0.013
O4	8	O-2	1.00	0.62492(25)	0.38365(34)	0.93653(14)	0.016
O5	8	O-2	1.00	0.43123(32)	0.73697(35)	0.80346(15)	0.016
O6	8	O-2	1.00	0.51148(24)	0.32971(33)	0.82401(13)	0.032
O7	8	O-2	1.00	0.36054(34)	0.59806(35)	0.92546(15)	0.005
C8	8	C	1.00	0.27040(30)	0.69828(36)	0.90334(22)	0.001
C9	8	C	1.00	0.31741(35)	0.78684(39)	0.82562(23)	0.017
C10	8	C	1.00	0.59579(34)	0.20583(39)	0.92517(15)	0.044
C11	8	C	1.00	0.52973(36)	0.17300(36)	0.85787(16)	0.049

^aSpace group, $Pcab$; lattice parameters, $a = 9.4687(1)$ Å, $b = 7.7711(1)$ Å, and $c = 19.5383(2)$ Å. The Rwp of the refinement is 3.13%.

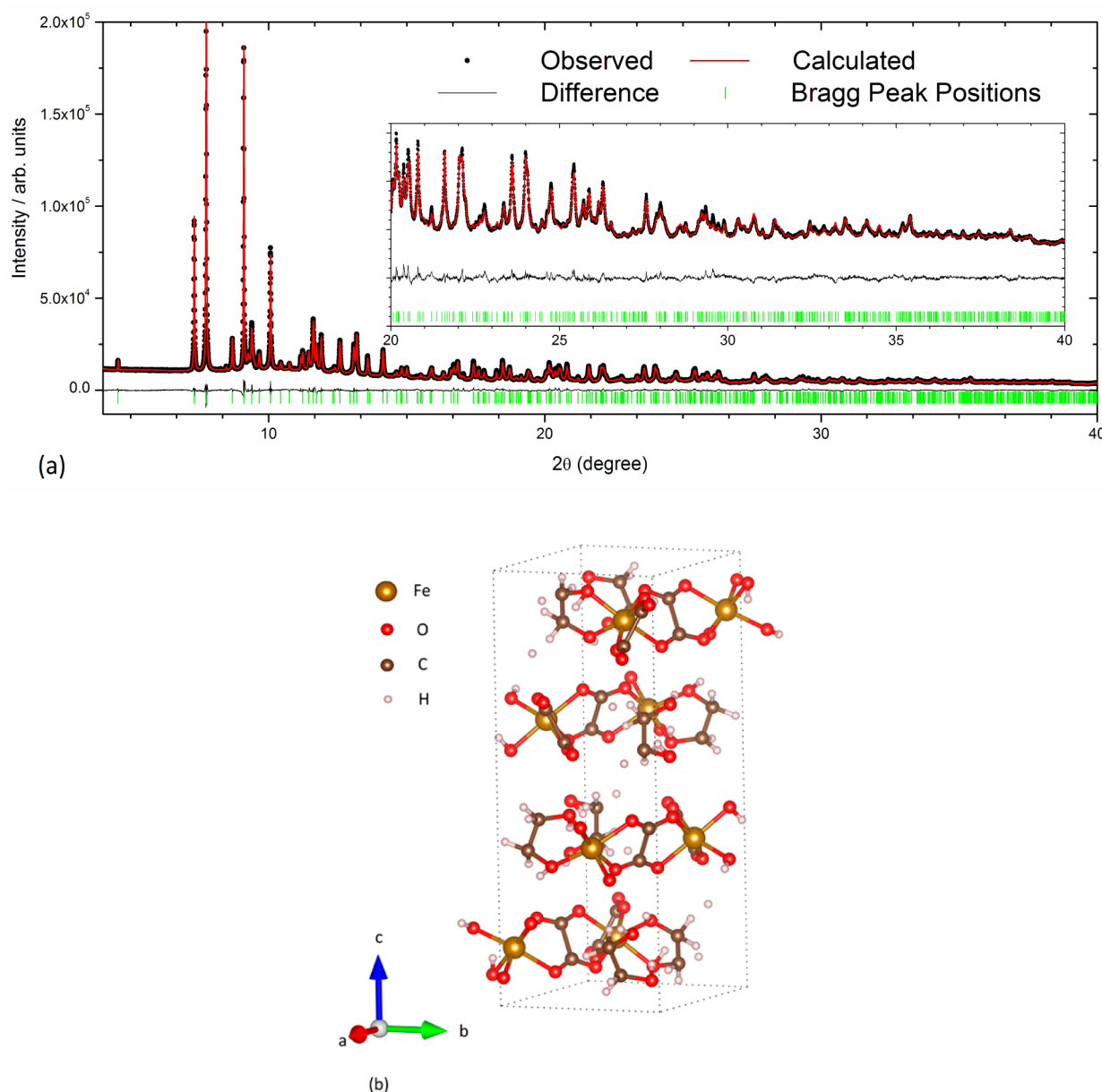


Figure 4. (a) Rietveld refinement of the powder diffraction pattern of the intermediate phase synthesized at 130 °C in an autoclave for 3 h. The XRD pattern was taken at room temperature. The X-ray wavelength is $\lambda = 0.77442$ Å. (b) The ball-and-stick model of the unit cell of the solved structure of ethylene glycol iron oxalate complex, $\text{FeC}_2\text{O}_4 \cdot \text{C}_2\text{H}_6\text{O}_2$.

to 150 °C for 18 h under ambient atmosphere.²⁰ They did not solve the crystal structure of the compound but determined its chemical formula by thermogravimetric analysis and IR spectroscopy to be $(\text{FeC}_2\text{O}_4 \cdot \text{C}_2\text{H}_6\text{O}_2)$, consistent with what we obtained from the EDX and XRD structure solution.

Reaction Pathway and Mechanisms. Formation of the $\text{FeC}_2\text{O}_4 \cdot \text{C}_2\text{H}_6\text{O}_2$ Intermediate. Structurally, the precursor $\text{FeC}_2\text{O}_4 \cdot 2\text{H}_2\text{O}$ consists of infinite chains formed by Fe^{2+} and $\text{C}_2\text{O}_4^{2-}$ along the *b*-axis, linked together by hydrogen bonds formed between the hydrogen of water molecules and oxygen from $\text{C}_2\text{O}_4^{2-}$. Compared to the precursor $\text{FeC}_2\text{O}_4 \cdot 2\text{H}_2\text{O}$, one EG molecule in $\text{FeC}_2\text{O}_4 \cdot \text{C}_2\text{H}_6\text{O}_2$ binds to Fe atoms as a bidentate ligand, replacing the two water molecules in the precursor. This scheme suggests that EG participates in the reaction directly via a ligand-exchange process. In $\text{FeC}_2\text{O}_4 \cdot 2\text{H}_2\text{O}$, the two water molecules bonding to the Fe ion align in a straight line perpendicular to the plane formed by the chainlike

$(\text{C}_2\text{O}_4)\text{—Fe—}(\text{C}_2\text{O}_4)$ moieties along the *b*-axis.²¹ After the ligand-exchange reaction, because the distance between the two oxygen atoms of bidentate EG is too short to ligate to the Fe ion in a 180° angle, it forms two coordinating bonds perpendicular to each other. Consequently, the $\text{—}(\text{C}_2\text{O}_4)\text{—Fe—}(\text{C}_2\text{O}_4)$ chains are no longer straight, but rather form a zigzag pattern, with an Fe—Fe—Fe angle of 117.8°.

Experimentally, we observed subtle structural changes in $\text{FeC}_2\text{O}_4 \cdot 2\text{H}_2\text{O}$ in terms of the Fe—Fe atomic distances and the chain—chain distances from room temperature to 90 °C (Figure S, left panel). As shown in the right panel of Figure S, D_a represents the chain—chain distance along the *a*-axis, D_b the in-chain Fe—Fe distance along the *b*-axis, and D_c the chain—chain distance along the *c*-axis, which is parallel to the hydrogen bonds formed between the water molecules and oxalate ions. With rising temperature, D_a increases at a rate about three times that of D_c , while D_b decreases with temperature.

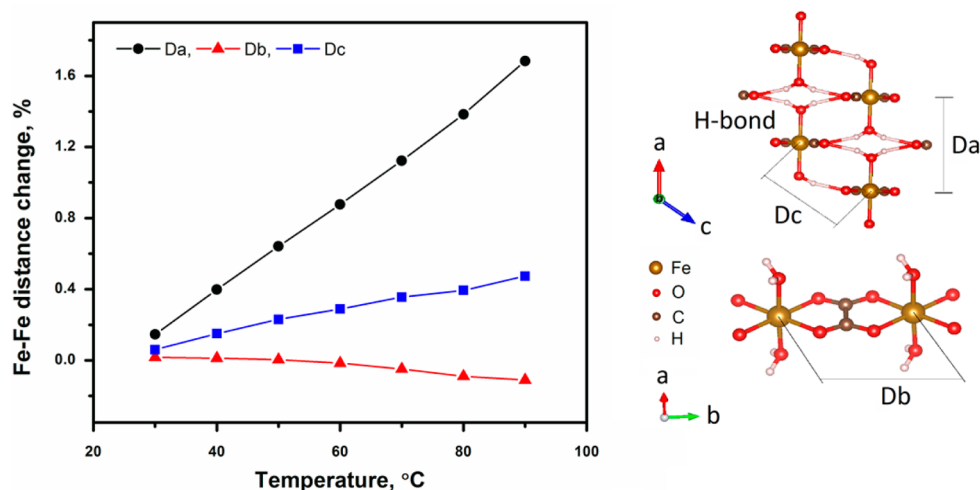


Figure 5. Variation in the in-chain Fe–Fe distance (D_b), and the chain–chain distances (D_a and D_c) with temperature of ferrous oxalate dihydrate, $\text{FeC}_2\text{O}_4 \cdot 2\text{H}_2\text{O}$.

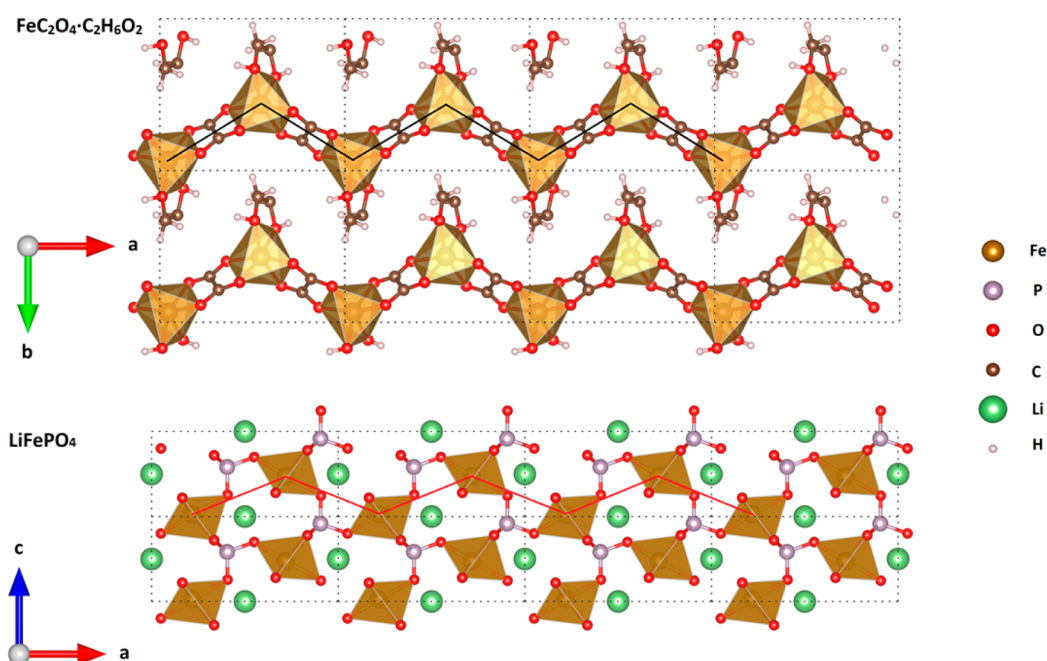


Figure 6. Structural similarities between the intermediate $\text{FeC}_2\text{O}_4 \cdot \text{C}_2\text{H}_6\text{O}_2$ (top) and the product LiFePO_4 (bottom). The FeO_6 octahedrons of LFP (brown in the lower part) and $\text{FeC}_2\text{O}_4 \cdot \text{C}_2\text{H}_6\text{O}_2$ (yellow in the upper part) assume a similar zigzag chain along the a -axis, as highlighted by the lines drawn between octahedrons. The Fe–Fe–Fe angle is 117.8° in $\text{FeC}_2\text{O}_4 \cdot \text{C}_2\text{H}_6\text{O}_2$ and 135.5° in LFP. The Fe–Fe distances is 5.529 \AA in $\text{FeC}_2\text{O}_4 \cdot \text{C}_2\text{H}_6\text{O}_2$ and 5.596 \AA in LFP.

Therefore, the highest rate of increase with temperature in D_a shows that the weakest bonding between the chains is along the a -axis. Similarly, the moderate increase of D_c indicates a weakening of the hydrogen bonds between the oxalate chains in the c -axis direction. Interestingly, the Fe–Fe distance along the b -axis declines with rising temperature, indicating enhanced strengthening of the in-chain bonds between Fe^{2+} and $\text{C}_2\text{O}_4^{2-}$, most likely due to the increase of effective charges on $\text{C}_2\text{O}_4^{2-}$ ions after the weakening of hydrogen bonding.

Based on the anisotropic response of the humboldtine lattice to temperature during its reaction with ethylene glycol, the ligand-exchange reaction may proceed via the following steps. First, with the increase of temperature, the distance between linear $-\text{Fe}-\text{C}_2\text{O}_4-\text{Fe}-\text{C}_2\text{O}_4-$ chains widens, which may generate free-standing chains surrounded by the EG solvent,

and the consequent dissolution of $\text{FeC}_2\text{O}_4 \cdot 2\text{H}_2\text{O}$. Second, the EG molecules, a bidentate ligand, attack the chain at the Fe–O bond between Fe– C_2O_4 or Fe– H_2O , replacing water with EG, breaking or rearranging the bonds between Fe and C_2O_4 moieties, and forming $\text{FeC}_2\text{O}_4 \cdot \text{C}_2\text{H}_6\text{O}_2$ clusters. Third, the $\text{FeC}_2\text{O}_4 \cdot \text{C}_2\text{H}_6\text{O}_2$ becomes highly concentrated in the ethylene glycol solution and precipitates when the solution is over-saturated. Overall, the transition from $\text{FeC}_2\text{O}_4 \cdot 2\text{H}_2\text{O}$ to $\text{FeC}_2\text{O}_4 \cdot \text{C}_2\text{H}_6\text{O}_2$ follows a dissolution–precipitation process.

From $\text{FeC}_2\text{O}_4 \cdot \text{C}_2\text{H}_6\text{O}_2$ Intermediate to LFP. Compared to $\text{FeC}_2\text{O}_4 \cdot 2\text{H}_2\text{O}$, the structure of $\text{FeC}_2\text{O}_4 \cdot \text{C}_2\text{H}_6\text{O}_2$ intermediate resembles the LFP product more closely. As Figure 6 shows, the FeO_6 octahedrons in both the intermediate and product phases form zigzag chains along the a -axis with a similar Fe–Fe–Fe angle: 117.8° for $\text{FeC}_2\text{O}_4 \cdot \text{C}_2\text{H}_6\text{O}_2$ and 135.5° for LFP.

The Fe–Fe distances also are similar: 5.529 Å in $\text{FeC}_2\text{O}_4 \cdot \text{C}_2\text{H}_6\text{O}_2$ and 5.596 Å in LFP. Because of stronger ionic bonding between Fe^{2+} and PO_4^{3-} , the FeO_6 are interlocked more compactly to each other in LFP, leading to a smaller molar volume of 44 cm^3/mol . In comparison, the molar volume of $\text{FeC}_2\text{O}_4 \cdot \text{C}_2\text{H}_6\text{O}_2$ is 108 cm^3/mol , much larger than that of LFP. Because of the much smaller molar volume of LFP relative to the intermediate, the transition from $\text{FeC}_2\text{O}_4 \cdot \text{C}_2\text{H}_6\text{O}_2$ to LFP may be an interface-coupled dissolution–reprecipitation (ICDR) process.²² During an ICDR process, a fluid boundary layer at the interface between the parent's solid phase (in the current case, $\text{FeC}_2\text{O}_4 \cdot \text{C}_2\text{H}_6\text{O}_2$) and the solvent is formed by the dissolution of the parent phase. Reactions between the dissolved $\text{FeC}_2\text{O}_4 \cdot \text{C}_2\text{H}_6\text{O}_2$ and LiH_2PO_4 occur within the boundary layer, forming less soluble LFP, which supersaturates the boundary layer and immediately reprecipitates at the interface. For the ICDR process to occur, relative to parent phase, the product phase must have a smaller unit-cell volume, lower solubility, but a higher structural similarity, and the $\text{FeC}_2\text{O}_4 \cdot \text{C}_2\text{H}_6\text{O}_2 \rightarrow \text{LFP}$ transition meets all these requirements. In contrast to the regular dissolution–precipitation process that features an Ostwald ripening process, or the growth in average crystal size with time and temperature, and independent of the size of parent phase, the crystallites formed via the interface-coupled dissolution–reprecipitation process assume their maximal sizes in a very short time (Figure 13a,c). Experimentally, we observed the gradual growth in crystal size during the formation of $\text{FeC}_2\text{O}_4 \cdot \text{C}_2\text{H}_6\text{O}_2$ but not during LFP formation, which supports this interface-coupled dissolution–reprecipitation mechanism.

Distortion of the FeO_6 Octahedron during Phase Transitions. During the two previously described phase transitions, the FeO_6 octahedrons are preserved in all three Fe-containing solid phases, but they behave differently because of different transition mechanisms. Therefore, it is interesting to probe the subtle intra- and inter- FeO_6 structural changes during heating to gain a deeper understanding. Here, we use average Fe–O bond lengths (Figure 7a) and an effective coordination number (ECN)²³ (Figure 7b) to characterize the intra- FeO_6 property and cell volume to gauge average inter- FeO_6 distances (Figure 7c). The ECN is defined as the summation of the “bond weight” of bonds between a center atom (Fe in this case) and a corner atom (O in this case) of a coordination polyhedron (FeO_6). For an FeO_6 octahedron, if all the Fe–O bond lengths are the same, then the ECN is 6. Any ECN value less than 6 measures the distortion of the FeO_6 octahedron. The values of ECN were extracted from the refined structure models using the structural visualization software VESTA.²⁴

At the beginning of ligand-exchange reaction, while the unit cell expands with the increase of temperature, the average Fe–O bond length in $\text{FeC}_2\text{O}_4 \cdot 2\text{H}_2\text{O}$ decreases and the ECN remains constant at 6, suggesting an overall weakening of the bonds between the FeO_6 octahedrons, just as it should be in a dissolution process. The intermediate phase $\text{FeC}_2\text{O}_4 \cdot \text{C}_2\text{H}_6\text{O}_2$ emerges with an average Fe–O bond length slightly greater than that of $\text{FeC}_2\text{O}_4 \cdot 2\text{H}_2\text{O}$. This average Fe–O bond length then decreases and stays constant in a narrow temperature window (between 100 and 140 °C), indicating the stabilization of the intermediate phase after the ligand-exchange reaction. The most notable feature during this reaction is that the ECN of FeO_6 in $\text{FeC}_2\text{O}_4 \cdot 2\text{H}_2\text{O}$ remains ~ 6 , further confirming a simple dissolution–reprecipitation process.

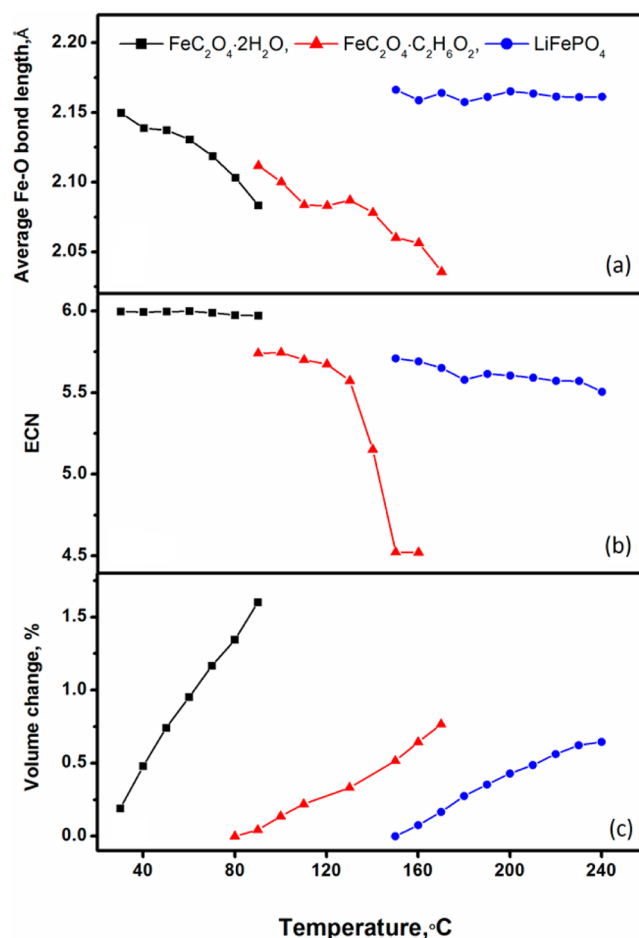


Figure 7. Temperature dependence of (a) average Fe–O bond length, (b) effective coordination number (ECN) of FeO_6 octahedrons, and (c) thermal expansion of the unit cell of ferrous oxalate dehydrate (black squares), EG ferrous oxalate complex (red triangles), and LiFePO_4 (blue circles) observed in the solvothermal synthesis.

In contrast, during the phase transition from $\text{FeC}_2\text{O}_4 \cdot \text{C}_2\text{H}_6\text{O}_2$ to LFP, the ECN of the FeO_6 in $\text{FeC}_2\text{O}_4 \cdot \text{C}_2\text{H}_6\text{O}_2$ dropped drastically from 5.7 to 4.5 when the LFP started to precipitate out at about 140 °C. A lower ECN number means increased distortion of the FeO_6 octahedron. Furthermore, it signifies that some Fe–O bond lengths will be much longer and therefore weaker and more chemically reactive. This drastic distortion possibly is due to the ICDR reaction in the boundary layer. The new Fe–O bonds of the FeO_6 octahedron in LiFePO_4 are, on average, $\sim 6\%$ longer than those in $\text{FeC}_2\text{O}_4 \cdot \text{C}_2\text{H}_6\text{O}_2$ in the same temperature range, but they change very little with temperature, so revealing the good structural stability of the FeO_6 polyhedra in LFP. The stability of FeO_6 in LFP in the EG solvent further is evidenced by the slow variation of the averaged ECN in LFP with temperature.

In summarizing, on the basis of the experimental evidence obtained from our in situ XRD measurements, we propose a two-step reaction mechanism for the synthesis of LFP (Figure 8). In the first step, the precursor phase $\text{FeC}_2\text{O}_4 \cdot 2\text{H}_2\text{O}$ is converted into $\text{FeC}_2\text{O}_4 \cdot \text{C}_2\text{H}_6\text{O}_2$ via a direct dissolution–precipitation process at a low temperature range. In the second step, with further increase of temperature, the intermediate $\text{FeC}_2\text{O}_4 \cdot \text{C}_2\text{H}_6\text{O}_2$ phase becomes unstable and transforms into the final LFP phase via an interface-coupled dissolution–reprecipitation process.

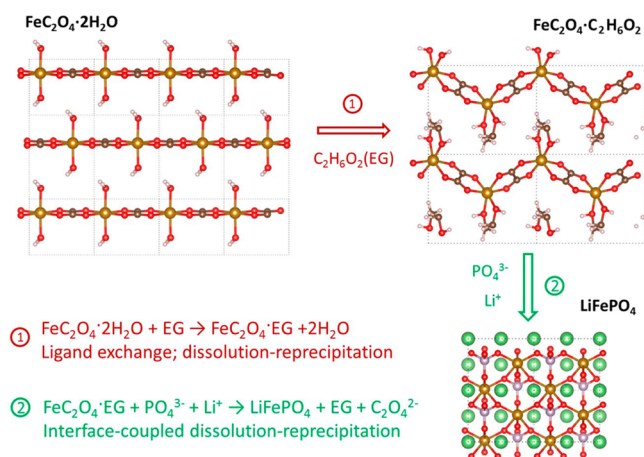


Figure 8. Schematic illustration of the two-step reaction process during solvothermal synthesis of LFP. In all ball-and-stick models, brown is for Fe, red for O, gray for C, green for Li, purple for P, and light pink for H. The size of the ball is not proportional to the size of the ions and atoms.

LiMnPO₄ Synthesis. Figure 9 shows the time-resolved XRD patterns acquired during the synthesis of LMP. At room

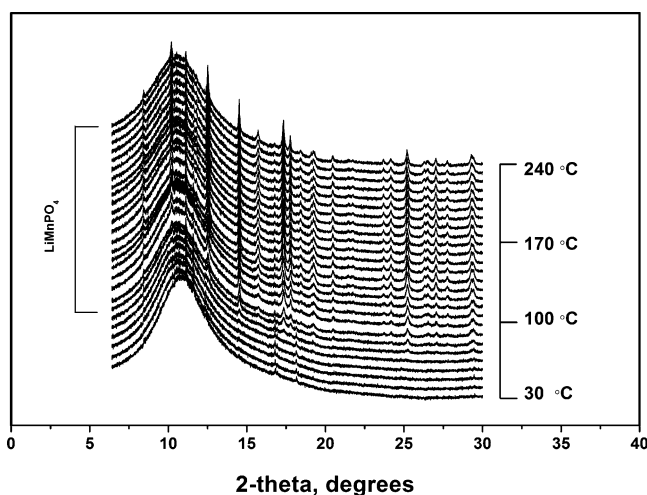


Figure 9. In situ XRD patterns of solvothermal synthesis of LiMnPO₄ in ethylene glycol solvent from room temperature to 240 °C. No intermediate phase was observed during the reaction. The X-ray wavelength is $\lambda = 0.77442 \text{ \AA}$.

temperature, there were no diffraction peaks from the precursors $(\text{CH}_3\text{COO})_2\text{Mn} \cdot 4\text{H}_2\text{O}$ and LiH_2PO_4 , indicating that they were fully dissolved in the EG solvent. At 80 °C, the olivine LiMnPO₄ was detected, and its diffraction peaks continuously grew with increasing temperature, which is evidence of a dissolution–precipitation process. The in situ XRD measurements reveal that the LMP's solvothermal synthesis follows a simple precipitation process, namely a transformation directly from precursor to final product without going through any intermediate phases, which is quite different from the process of LFP formation. The crystal size and the unit cell volume of LMP increased with temperature, but a reduction in the rate of cell volume expansion was observed at 150 °C, suggesting an emerging reduction in volume that competes with thermal expansion. The reduction of the unit cell's volume most probably is due to the elimination of antisite

defects during crystal growth at elevated temperatures, similar to the phenomena observed in the hydrothermal synthesis of LiFePO₄.¹⁸

LiFe_{0.4}Mn_{0.6}PO₄ Synthesis. LiFe_{0.4}Mn_{0.6}PO₄ was synthesized in situ using a mixture of precursors that were used in the syntheses of LiFePO₄ and LiMnPO₄, with a nominal molar ratio of 4:6 between Fe²⁺ and Mn²⁺ ions. By analyzing the in situ XRD data, we found that the synthesis of Li(Fe, Mn)PO₄ is not a simple addition of the LFP and LMP processes. As shown in Figure 10, similar to the observation in the synthesis of

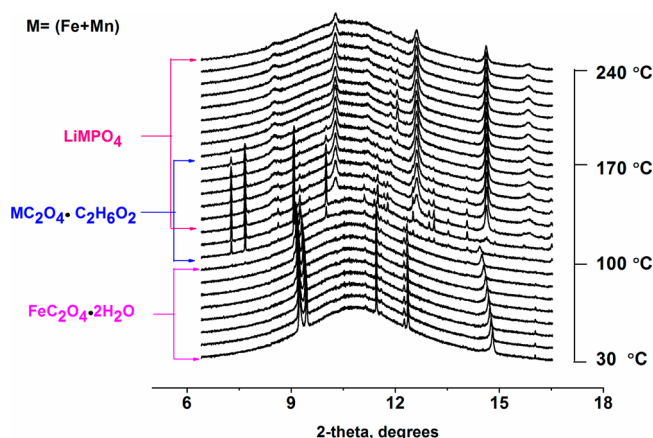


Figure 10. In situ XRD patterns of solvothermal synthesis of Li(Fe, Mn)PO₄ in ethylene glycol solvent from room temperature to 240 °C. The Fe/Mn molar ratio is 2/3 in the starting materials. The presence of the precursor $\text{FeC}_2\text{O}_4 \cdot 2\text{H}_2\text{O}$, intermediate phase, and Li(Fe, Mn)PO₄ are marked. The X-ray wavelength is $\lambda = 0.77442 \text{ \AA}$.

LiFePO₄, there also is an intermediate phase in the formation of LFMP. However, during the reactions leading to LiFePO₄, the intermediate phase formed at 60 °C, but for Li(Fe, Mn)PO₄, it formed at ~100 °C, indicating that the reaction requires a higher activation energy. The final olivine phase also appeared at different temperatures, i.e., 80 °C for LiMnPO₄, 110 °C for Li(Fe, Mn)PO₄, and 140 °C for LiFePO₄.

The intermediate phase formed in LFMP synthesis has a structure similar to that of $\text{FeC}_2\text{O}_4 \cdot \text{C}_2\text{H}_6\text{O}_2$ observed in the synthesis of LFP (shown in Figure 10), but with a unit cell 1% larger in volume (Figure 11) that suggests the formation of an $(\text{Fe,Mn})\text{C}_2\text{O}_4 \cdot \text{C}_2\text{H}_6\text{O}_2$ solid solution by incorporating bigger Mn²⁺ ions. For a better comparison, the two in situ XRD patterns from LFP and LFMP processes, both taken at 120 °C, with major contribution from the intermediate phases, are plotted in Figure S4 in Supporting Information. The final product, LFMP, is a single olivine phase with a unit cell volume between those of LFP and LMP and therefore is a solid solution of these two. This is confirmed by Figure S5 in Supporting Information, which compares the XRD patterns of the three product phases, LFP, LMP, and LFMP, taken at 240 °C. It clearly shows that the product of the LFMP process is a single phase with lattice parameters that fall between those of the two end phases. Apparently, the intermediate solid solution $(\text{Fe,Mn})\text{C}_2\text{O}_4 \cdot \text{C}_2\text{H}_6\text{O}_2$ is the key to the formation of the LFMP solid solution. There are three possible competing reaction paths in this system:

1. The formation of LFP in a two-step process via the $\text{FeC}_2\text{O}_4 \cdot \text{C}_2\text{H}_6\text{O}_2$ intermediate, the same as that detailed in LiFePO₄ Synthesis.

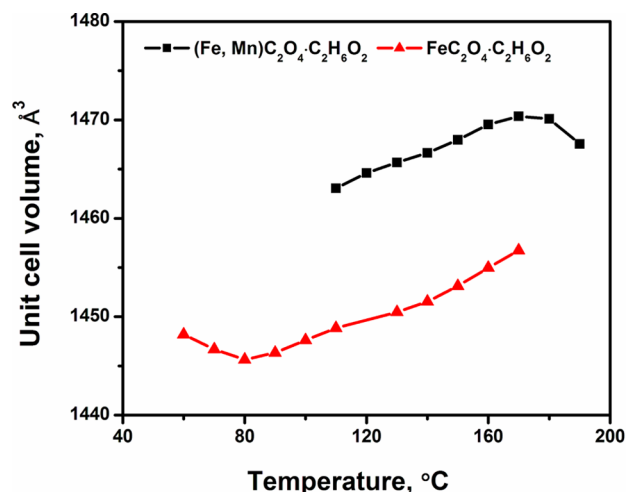


Figure 11. Temperature-dependent changes in the unit cell volume of the intermediate phase during solvothermal synthesis of LiFePO_4 and Li(Fe, Mn)PO_4 . The larger unit cell of $(\text{Fe, Mn})\text{C}_2\text{O}_4\cdot\text{C}_2\text{H}_6\text{O}_2$ relative to $\text{FeC}_2\text{O}_4\cdot\text{C}_2\text{H}_6\text{O}_2$ indicates the incorporation of Mn ions into the intermediate complex.

2. The direct formation of LMP without any intermediate, as described in LiMnPO_4 Synthesis.
3. The formation of the LFMP solid solution via the $(\text{Fe, Mn})\text{C}_2\text{O}_4\cdot\text{C}_2\text{H}_6\text{O}_2$ solid solution intermediate.

If either process 1 or 2 or both occur, the final product would not be a single phase but a mix of at least two phases. Because only a single olivine phase was experimentally observed, these two reaction paths were suppressed by path 3, i.e., the formation of the $(\text{Fe, Mn})\text{C}_2\text{O}_4\cdot\text{C}_2\text{H}_6\text{O}_2$ solid solution intermediate.

From Figure 12 it is apparent that the transition from the intermediate to the product is a kinetically fast process. Once $(\text{Fe, Mn})\text{C}_2\text{O}_4\cdot\text{C}_2\text{H}_6\text{O}_2$ is formed, it is quickly converted to

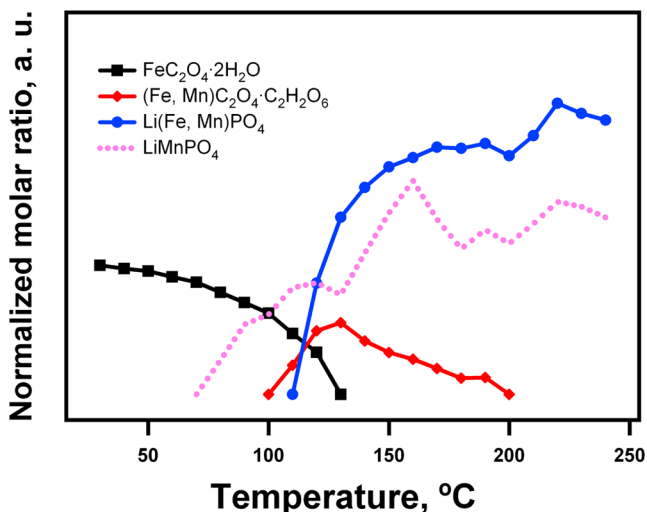


Figure 12. Normalized molar ratio of detectable crystalline phases during the solvothermal synthesis of Li(Fe, Mn)PO_4 from room temperature to 240°C in ethylene glycol. Shown are the precursor $\text{FeC}_2\text{O}_4\cdot 2\text{H}_2\text{O}$ (black squares), the intermediate phase $(\text{Fe, Mn})\text{C}_2\text{O}_4\cdot\text{C}_2\text{H}_6\text{O}_2$ (red diamonds), and the product Li(Fe, Mn)PO_4 (blue circles). The pink dotted line represents the formation of LiMnPO_4 without the presence of $\text{FeC}_2\text{O}_4\cdot 2\text{H}_2\text{O}$.

LFMP, leading to much higher phase fraction of the latter relative to the intermediate. With its relatively slower production and faster consumption, the quantity of the intermediate phase can never reach the amount of the initial precursor. After the phase fraction of the intermediate has peaked, the rate of the formation for the final product slows. Upon the complete consumption of the intermediate phase, the quantity of the final product was close to that of the combination of Fe and Mn in the precursors, suggesting that they both were completely incorporated into the final LFMP solid solution.

Figure 13 compares the evolutions of crystal sizes over time and temperature in the three reaction processes. The averaged

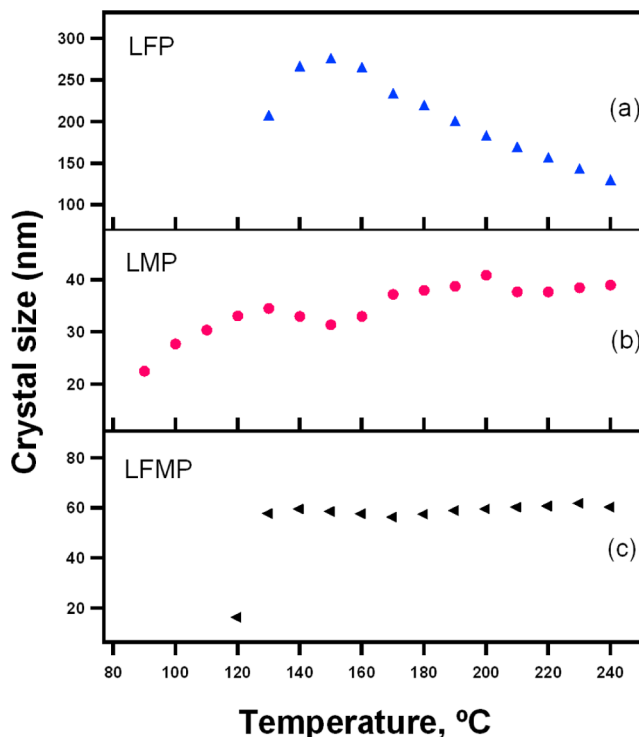


Figure 13. Evolution of crystal sizes with increasing temperature in the three reaction processes, (a) LFP, (b) LMP, and (c) LFMP.

crystal sizes were derived from the Rietveld refinements of the in situ XRD patterns (Figures 2, 9, and 10 and Figure S5 in Supporting Information). The LFP and LFMP synthetic processes, shown in panels a and c of Figure 13, respectively, both feature the sudden formation of crystals to their maximal sizes in the product phases, while in the LMP process, shown in Figure 13b, which assumes a dissolution–precipitation mechanism, the crystal size gradually increases over the entire course of synthesis (Ostwald ripening). This observation supports the conclusion that the Li(Fe, Mn)PO_4 solid solution phase is formed in a two-step process similar to that of LiFePO_4 , through the $(\text{Fe, Mn})\text{C}_2\text{O}_4\cdot\text{C}_2\text{H}_6\text{O}_2$ intermediate in an interface-coupled reaction. The crystal size starts declining after reaching the maximum in the LFP process (Figure 13a) accompanied by a decline in the product phase's molar ratio (Figure 3), suggesting a partial dissolution phenomenon discussed earlier.

CONCLUSIONS

Our systematic in situ XRD investigations of solvothermal synthesis of LiFePO_4 , LiMnPO_4 , and $\text{Li}(\text{Mn,Fe})\text{PO}_4$ from $\text{FeC}_2\text{O}_4 \cdot 2\text{H}_2\text{O}$ and $\text{Mn}(\text{Ac})_2 \cdot 4\text{H}_2\text{O}$ in an ethylene glycol solvent revealed the following significant reaction mechanisms:

Two phase transitions were involved in the formation of LiFePO_4 , with a newly discovered orthorhombic intermediate phase $\text{FeC}_2\text{O}_4 \cdot \text{C}_2\text{H}_6\text{O}_2$. The first phase transition from precursor to intermediate is a ligand-exchange reaction following a dissolution–reprecipitation process. The second phase transition, from intermediate to product, is an interface-coupled dissolution–reprecipitation process due to the structures' similarity but the large difference in unit-cell volume between $\text{FeC}_2\text{O}_4 \cdot \text{C}_2\text{H}_6\text{O}_2$ and LiFePO_4 .

No intermediate phase was observed from in situ XRD data during LiMnPO_4 synthesis; seemingly, it is a single-step precipitation. However, when the $\text{FeC}_2\text{O}_4 \cdot 2\text{H}_2\text{O}$ precursor also was present, the formation of LMP was suppressed. Instead, an intermediate phase that is isostructural to $\text{FeC}_2\text{O}_4 \cdot \text{C}_2\text{H}_6\text{O}_2$ but with a larger unit cell was observed, indicating that both Fe and Mn had been incorporated into the intermediate and formed a $(\text{Fe,Mn})\text{C}_2\text{O}_4 \cdot \text{C}_2\text{H}_6\text{O}_2$ solid solution. This $(\text{Fe,Mn})\text{C}_2\text{O}_4 \cdot \text{C}_2\text{H}_6\text{O}_2$, kinetically fast in its conversion to a more stable LFMP final product, suppressed the production of LFP and LMP, ensuring the generation of a $\text{Li}(\text{Mn, Fe})\text{PO}_4$ solid solution instead of a mixture of LFP and LMP.

Our findings about the reaction mechanism of solvothermal synthesis of olivine structured metal phosphates will guide us to further developments of cathode materials for the next generation of lithium-ion batteries. The in situ XRD method developed in this work offers a new way of exploring a wide range of solvothermal synthesis reactions and will find wide application in the rational design of new battery electrodes and other functional materials.

ASSOCIATED CONTENT

Supporting Information

SEM images and galvanostatic cycling performance of the synthesized $\text{LiFe}_x\text{Mn}_{1-x}\text{PO}_4$ and in situ XRD patterns comparing the intermediate phases of LFP and LFMP and product phases of LFP, LFMP, and LMP. This material is available free of charge via the Internet at <http://pubs.acs.org>.

AUTHOR INFORMATION

Corresponding Author

*Brookhaven National Laboratory, Photon Science Directorate, Bldg. 741, Upton, NY 11973. E-mail: jmbai@bnl.gov. Tel.: (631)-344-2583.

Present Address

[†]J.G.: HRL Laboratories, LLC, 3011 Malibu Canyon Road, Malibu, CA 90265-4797.

Notes

The authors declare no competing financial interest.

ACKNOWLEDGMENTS

This work is supported by the U.S. Department of Energy, Office of Energy Efficiency and Renewable Energy (DOE-EERE) under the Batteries for Advanced Transportation Technologies (BATT) Program, under Contract DE-AC02-98CH10886. Use of the National Synchrotron Light Source, Brookhaven National Laboratory, was supported by the U.S.

Department of Energy, Office of Science, Office of Basic Energy Sciences, under Contract DE-AC02-98CH10886.

REFERENCES

- (1) Padhi, A. K.; Nanjundaswamy, K. S.; Goodenough, J. B. Phospho-olivines as Positive-Electrode Materials for Rechargeable Lithium Batteries. *J. Electrochem. Soc.* **1997**, *144*, 1188–1194.
- (2) Yamada, A.; Hosoya, M.; Chung, S. C.; Kudo, Y.; Hinokuma, K.; Liu, K. Y.; Nishi, Y. Olivine-type Cathodes: Achievements and Problems. *J. Power Sources* **2003**, *119*, 232–238.
- (3) Chung, S. Y.; Bloking, J. T.; Chiang, Y. M. Electronically Conductive Phospho-olivines as Lithium Storage Electrodes. *Nat. Mater.* **2002**, *1*, 123–128.
- (4) Kang, B.; Ceder, G. Battery Materials for Ultrafast Charging and Discharging. *Nature* **2009**, *458*, 190–193.
- (5) Yang, S. F.; Song, Y. N.; Ngala, K.; Zavalij, P. Y.; Whittingham, M. S. Performance of LiFePO_4 as Lithium Battery Cathode and Comparison with Manganese and Vanadium Oxides. *J. Power Sources* **2003**, *119*, 239–246.
- (6) Zhou, X.; Wang, F.; Zhu, Y.; Liu, Z. Graphene Modified LiFePO_4 Cathode Materials for High Power Lithium Ion Batteries. *J. Mater. Chem.* **2011**, *21*, 3353–3358.
- (7) Hu, L. H.; Wu, F. Y.; Lin, C. T.; Khlobystov, A. N.; Li, L. J. Graphene-modified LiFePO_4 Cathode for Lithium Ion Battery Beyond Theoretical Capacity. *Nat. Commun.* **2013**, *4*, Article number 1687.
- (8) Zhang, S.; Meng, F. L.; Wu, Q.; Liu, F. L.; Gao, H.; Zhang, M.; Deng, C. Synthesis and Characterization of LiMnPO_4 Nanoparticles Prepared by a Citric Acid Assisted Sol-Gel Method. *Int. J. Electrochem. Sci.* **2013**, *8*, 6603–6609.
- (9) Delacourt, C.; Laffont, L.; Bouchet, R.; Wurm, C.; Leriche, J. B.; Morcrette, M.; Tarascon, J. M.; Masquelier, C. Toward Understanding of Electrical Limitations (Electronic, Ionic) in LiMPO_4 ($\text{M} = \text{Fe, Mn}$) Electrode Materials. *J. Electrochem. Soc.* **2005**, *152*, A913–A921.
- (10) Delacourt, C.; Poizot, P.; Morcrette, M.; Tarascon, J. M.; Masquelier, C. One-Step Low-Temperature Route for the Preparation of Electrochemically Active LiMnPO_4 Powders. *Chem. Mater.* **2004**, *16*, 93–99.
- (11) Hong, J. A.; Wang, F.; Wang, X. L.; Graetz, J. $\text{LiFe}_x\text{Mn}_{1-x}\text{PO}_4$: A Cathode for Lithium-ion Batteries. *J. Power Sources* **2011**, *196*, 3659–3663.
- (12) Martha, S. K.; Grinblat, J.; Haik, O.; Zinigrad, E.; Drezen, T.; Miners, J. H.; Exnar, I.; Kay, A.; Markovsky, B.; Aurbach, D. $\text{LiMn}_{0.8}\text{Fe}_{0.2}\text{PO}_4$: An Advanced Cathode Material for Rechargeable Lithium Batteries. *Angew. Chem., Int. Ed.* **2009**, *48*, 8559–8563.
- (13) Oh, S. M.; Myung, S. T.; Choi, Y. S.; Oh, K. H.; Sun, Y. K. Co-precipitation Synthesis of Micro-sized Spherical $\text{LiMn}_{0.5}\text{Fe}_{0.5}\text{PO}_4$ Cathode Material for Lithium Batteries. *J. Mater. Chem.* **2011**, *21*, 19368–19374.
- (14) Chen, J. J.; Vacchio, M. J.; Wang, S. J.; Chernova, N.; Zavalij, P. Y.; Whittingham, M. S. The Hydrothermal Synthesis and Characterization of Olivines and Related Compounds for Electrochemical Applications. *Solid State Ionics* **2008**, *178*, 1676–1693.
- (15) Saravanan, K.; Ramar, V.; Balaya, P.; Vittal, J. J. $\text{Li}(\text{Mn}_x\text{Fe}_{1-x})\text{PO}_4/\text{C}$ ($x = 0.5, 0.75$ and 1) Nanoplates for Lithium Storage Application. *J. Mater. Chem.* **2011**, *21*, 14925–14935.
- (16) Wang, L.; He, X. M.; Sun, W. T.; Wang, J. L.; Li, Y. D.; Fan, S. S. Crystal Orientation Tuning of LiFePO_4 Nanoplates for High Rate Lithium Battery Cathode Materials. *Nano Lett.* **2012**, *12*, 5632–5636.
- (17) Qin, X.; Wang, X. H.; Xiang, H. M.; Xie, J.; Li, J. J.; Zhou, Y. C. Mechanism for Hydrothermal Synthesis of LiFePO_4 Platelets as Cathode Material for Lithium-Ion Batteries. *J. Phys. Chem. C* **2010**, *114*, 16806–16812.
- (18) Chen, J. J.; Bai, J. M.; Chen, H. Y.; Graetz, J. In Situ Hydrothermal Synthesis of LiFePO_4 Studied by Synchrotron X-ray Diffraction. *J. Phys. Chem. Lett.* **2011**, *2*, 1874–1878.
- (19) Lim, J.; Gim, J.; Kang, S. W.; Baek, S.; Jeong, H.; Kim, J. Synthesis of LiFePO_4 Nanoparticles and Crystal Formation Mechanism during Solvothermal Reaction. *J. Electrochem. Soc.* **2012**, *159*, A479–A484.

(20) Krasil'nikov, V. N.; Gyrdasova, O. I.; Bazuev, G. V. Ethylene Glycol-Modified Cobalt and Iron Oxalates As Precursors for the Synthesis of Oxides As Extended Microsized and Nanosized Objects. *Russ. J. Inorg. Chem.* **2008**, *53*, 1854–1861.

(21) Echigo, T.; Kimata, M. Single-crystal X-ray Diffraction and Spectroscopic Studies on Humboldtine and Lindbergite: Weak Jahn–Teller Effect of Fe^{2+} ion. *Phys. Chem. Miner.* **2008**, *35*, 467–473.

(22) Putnis, A.; Putnis, C. V. The Mechanism of Reequilibration of Solids in the Presence of a Fluid Phase. *J. Solid State Chem.* **2007**, *180*, 1783–1786.

(23) Hoppe, R. Effective Coordination Numbers (ECoN) and Mean Fictive Ionic-RADII (MEFIR). *Z. Kristallogr.* **1979**, *150*, 23–52.

(24) Momma, K.; Izumi, F. VESTA 3 for Three-dimensional Visualization of Crystal, Volumetric and Morphology Data. *J. Appl. Crystallogr.* **2011**, *44*, 1272–1276.